The Astrophysical Journal Letters, 1000:L10 (13pp), 2026 March 20 https://doi.org/10.3847/2041-8213/ae4344

An Overabundance of Radio Active Galactic Nuclei in the SPT2349–56 Protocluster: Preheating the Intracluster Medium

Scott C. Chapman[1,2,3,4], Roger P. Deane[5,6], Dazhi Zhou[3], Manuel Aravena[7], William Rasakanya[5], Melanie Archipley[8,9], James Burgoyne[10], Jared Cathey[11], Anthony H. Gonzalez[11], Ryley Hill[3], Chayce Hughes[3], Mònica Natalia Isla Llave[12,13], Matt Malkan[14], Kedar A. Phadke[15,16,17], Vismaya Pillai[3], Ana Posses[18], Bonnie Slocombe[3], Manuel Solimano[19], Justin Spilker[18], Nikolaus Sulzenauer[20], Fabio Vito[12], Joaquin D. Vieira[15,16], David Vizgan[15], George Wang[3], and Axel Weiss[20]

[1] Department of Physics and Atmospheric Science, Dalhousie University, Halifax, NS, B3H 4R2, Canada; scott.chapman@dal.ca
[2] NRC Herzberg Astronomy and Astrophysics, 5071 West Saanich Road, Victoria, BC, V9E 2E7, Canada
[3] Department of Physics and Astronomy, University of British Columbia, Vancouver, BC, V6T1Z1, Canada
[4] Eureka Scientific Inc, Oakland, CA 94602, USA
[5] Wits Centre for Astrophysics, School of Physics, University of the Witwatersrand, 1 Jan Smuts Avenue, Johannesburg, 2000, South Africa
[6] Department of Physics, University of Pretoria, Private Bag X20, Pretoria 0028, South Africa
[7] Núcleo de Astronomia, Facultad de Ingenieria y Ciencias, Universidad Diego Portales, Av. Ejército 441, Santiago, Chile
[8] Department of Astronomy and Astrophysics, University of Chicago, 5640 South Ellis Avenue, Chicago, IL, 60637, USA
[9] Kavli Institute for Cosmological Physics, University of Chicago, 5640 South Ellis Avenue, Chicago, IL 60637, USA
[10] Department of Physics and Astronomy, University of Victoria, Victoria, Canada
[11] Department of Astronomy, University of Florida, 211 Bryant Space Science Center, Gainesville, FL 32611-2055, USA
[12] INAF—Osservatorio di Astrofisica e Scienza dello Spazio di Bologna (OAS), Via Gobetti 93/3, I-40129 Bologna, Italy
[13] Dipartimento di Fisica e Astronomia (DIFA), Università di Bologna, via Gobetti 93/2, I-40129 Bologna, Italy
[14] University of California Los Angeles, Department of Physics and Astronomy, 430 Portola Plaza, Los Angeles, CA 90095, USA
[15] Department of Astronomy, University of Illinois, 1002 West Green Street., Urbana, IL 61801, USA
[16] Center for AstroPhysical Surveys, National Center for Supercomputing Applications, 1205 West Clark Street, Urbana, IL 61801, USA
[17] NSF—Simons AI Institute for the Sky (SkAI), 172 E. Chestnut Street, Chicago, IL 60611, USA
[18] Department of Physics and Astronomy and George P. and Cynthia Woods Mitchell Institute for Fundamental Physics and Astronomy, Texas A&M University, 4242 TAMU, College Station, TX 77843-4242, USA
[19] Centro de Astrobiología (CAB), CSIC-INTA, Ctra. de Ajalvir km 4, Torrejón de Ardoz, E-28850, Madrid, Spain
[20] Max-Planck-Institut für Radioastronomie, Auf dem Hugel 69, Bonn, D-53121, Germany
Received 2025 November 21; revised 2026 February 3; accepted 2026 February 7; published 2026 March 11

Abstract

Following the detection of a radio-loud active galactic nucleus (AGN) in the $z = 4.3$ protocluster SPT2349−56, we have obtained additional observations with the South African MeerKAT radio telescope in the *S* band (2.4 GHz) with the aim of further characterizing radio emission from amongst the ∼30 submillimeter galaxies (SMGs) identified in the structure. In addition to the previous radio-AGN, we newly identify two of the protocluster SMGs individually at 2.4 GHz as having a radio excess. Two of these radio-AGN are now known to be X-ray luminous AGN. Two additional members are also detected with radio emission consistent with their star formation rate (SFR). Archival MeerKAT Ultra-High Frequency (UHF; 816 MHz) observations further constrain luminosities and radio spectral indices of these five galaxies. The Australia Telescope Compact Array is used to detect and resolve the central two sources at 5.5 and 9.0 GHz finding elongated, bipolar jet-like morphologies. The excess radio luminosities range from $L_{1.4,\mathrm{rest}} = (1\text{–}20) \times 10^{25}$ W Hz^{-1}, ∼10–100× higher than expected from the SFRs, assuming the usual far-infrared–radio correlation. Of the known cluster members, only the SMG "N1" shows signs of AGN in any other diagnostics, namely a large and compact excess in ^{12}CO(11–10) line emission. We compare these results to field samples of radio sources and SMGs. The overdensity of radio-loud AGN in the compact core region of the cluster may be providing significant heating to the recently discovered nascent intracluster medium in SPT2349−56.

Unified Astronomy Thesaurus concepts: Extragalactic radio sources (508); Radio galaxies (1343); Radio continuum emission (1340); AGN host galaxies (2017); Starburst galaxies (1570); Brightest cluster galaxies (181); Galaxy clusters (584); Protoclusters (1297)

1. Introduction

Protoclusters of galaxies, the precursors of established clusters, exhibit a reversal of the morphology–density relation seen in clusters at $z < 1$ (e.g., A. Dressler 1980; M. Postman et al. 2005), whereby star-forming galaxies are found in abundance in the central cluster regions (e.g., D. Elbaz et al. 2007). The active galactic nuclei (AGN) also tend to be more enhanced and numerous in massive protoclusters at redshifts around 2–3, compared to the general field environment or lower-redshift clusters (e.g., L. Pentericci et al. 2002; B. D. Lehmer et al. 2009; J. A. Digby-North et al. 2010). This increased AGN activity appears to be correlated with higher rates of star formation among galaxies in these protoclusters (e.g., S. C. Chapman et al. 2009; M. Brodwin et al. 2013; C. M. Casey et al. 2015; R. Gilli et al. 2019).

At low-to-moderate redshifts ($z < 1$), both AGN and star formation are largely suppressed in cluster galaxies (G. Kauffmann et al. 2004; P. Martini et al. 2006; C. van Breukelen et al. 2009;

J. Rasmussen et al. 2012; S. Ehlert et al. 2014). Both mechanical and radiative feedback mechanisms are invoked to accomplish this suppression, which are naturally produced by AGN. Supporting this, extended X-ray emission observed in some clusters reveals cavities or empty regions in the hot gas, which are consistent with shocked gas caused by AGN feedback (e.g., A. C. Fabian 2012).

In the high-redshift Universe, however, galaxy overdensities have abundant reservoirs of cold gas to supply star formation, and the ongoing mergers between galaxies expected in the dense environments provide triggers for star formation. Mergers can also provide the tidal torques necessary for the gas to overcome its angular momentum and fall to the accretion disk of the supermassive black hole (SMBH; J. M. Gabor et al. 2016). Examples at high redshift abound. In the MQN01 protocluster at $z = 3.25$, the AGN fraction from X-ray is significantly higher (>20%) than in the field and increases with stellar masses, reaching a value of 100% for $M^* > 3.2 \times 10^{10} M_\odot$ (A. Travascio et al. 2025). The $z = 3.09$ SSA22 protocluster identifies 50% of the SMGs hosting X-ray-luminous AGN (H. Umehata et al. 2019)—a clear excess over the 15% found for field SMGs (e.g., S. X. Wang et al. 2013). At even higher redshifts, the situation is less clear. Two recent discoveries of $z \sim 4$ star-forming cluster cores (T. B. Miller et al. 2018; I. Oteo et al. 2018) exhibit the highest overdensities in SFR ever found in the Universe, yet do not obviously show elevated AGN fractions compared to the field. In the case of the Distant Red Core (DRC) protocluster (I. Oteo et al. 2018), the overdensity of 10 SMGs found by the Hershel Space Telescope at $z = 4.0$ has been studied by Chandra in the X-ray (F. Vito et al. 2020) and in the radio (I. Oteo et al. 2018), revealing no significant excess of AGN activity in the system over field SMGs (22% versus 15%, respectively). Similarly, in the SPT2349−56 protocluster at $z = 4.3$ (T. B. Miller et al. 2018), two X-ray AGN were identified (F. Vito et al. 2024), with one of them also being radio-loud (S. C. Chapman et al. 2024), nominally an even lower AGN fraction in the SMGs (∼10%).

The X-ray properties observed in the intracluster medium (ICM) of nearby galaxy clusters often do not match what we would expect based solely on gravitational collapse. This suggests that additional sources of energy are at play, such as star-forming galaxies and AGN releasing energy into the ICM through outflows, to help to explain these observations (T. J. Ponman et al. 1999; P. Tozzi & C. Norman 2001). In cosmological simulations, this extra energy is often incorporated by tuning the effects of galactic winds driven by supernovae or AGN activity to match the properties we see locally (e.g., A. M. C. Le Brun et al. 2014; S. R. Pike et al. 2014). The most successful models suggest that most of this heating occurs early in the Universe's history (K. K. S. Wu et al. 2000), but many details remain uncertain based on observations. For example, the details are still debated about when this heating happens, how long it lasts, what the main energy sources are, and how the energy is transferred to the ICM (e.g., B. R. McNamara & P. E. J. Nulsen 2007; A. C. Fabian 2012). If this process were common at high redshifts, then energetic events like radio-AGN activity could have played a key role in determining the final energy state of galaxy clusters we observe today.

Recently, D. Zhou et al. (2026) identified an immense reservoir of thermal energy in SPT2349−56 through the detection of a strong Sunyaev–Zeldovich (SZ) decrement. In energetic terms, the signal is so strong that likely only radio AGN can provide the required feedback energy input through radio jet mechanical energy, heating an implied hot ICM component of the cluster gas to temperatures exceeding 1.7×10^7 K. This result is supported by a massive excess of cold molecular gas found in SPT2349−56, not obviously associated with the individual galaxies (D. Zhou et al. 2025). This cold gas was hypothesized to be a nascent ICM component, revealing that a massive body of gas is presently being heated by both AGN and gravitational collapse.

This Letter presents a search for additional radio detections of members of the SPT2349−56 cluster, with new *S*-band MeerKAT data, further analysis of the UHF MeerKAT data from S. C. Chapman et al. (2024), and new deep 5.5 and 9 GHz ATCA data. Section 2 describes the radio observations. Section 3 presents the results derived from the source extraction and analysis. In Section 4, we discuss the overdensity of radio sources and the implications for cluster evolution. Throughout our analysis, a Hubble constant of $H_0 = 70\,\mathrm{km\,s^{-1}\,Mpc^{-1}}$ and density parameters of $\Omega_\Lambda = 0.7$ and $\Omega_\mathrm{m} = 0.3$ are assumed, resulting in a proper angular scale of 6.88 kpc arcsec^{-1} at $z = 4.3$.

2. Data

2.1. MeerKAT Observations and Data Processing

2.1.1. MeerKAT 2.4 GHz Data

Observations with the MeerKAT radio telescope (J. Jonas & MeerKAT Team 2016) were carried out on SPT2349−56 in the *S* band, as part of a survey of eight $z > 4$ protocluster fields selected by South Pole Telescope (SPT; Program ID: SCI-20230907-SC-01, PI: Chapman). The *S* band covers a usable range of 1.96–3.50 GHz, and we selected the S1 subband ranging between 1968.75 and 2843.75 MHz. The 875 MHz of digitized bandwidth is split into 4096 channels, each 214 kHz wide and a correlator dump time of 8 s. The observations were carried out on 2023 December 21 with a total of 59 of the 64 antennas participating. A total of six 19.5 minute scans (1.95 hr on-source) were carried out, interleaved with other protocluster sources to maximize the *uv*-coverage and achieved angular resolution on SPT2349−56. A single pointing was centered on the target at $(\alpha, \delta) = 23^\mathrm{h}49^\mathrm{m}42\overset{\mathrm{s}}{.}5$, $-56^\mathrm{d}38^\mathrm{m}22\overset{\mathrm{s}}{.}5$. The absolute flux and bandpass calibrator was J 0408−6545. Time-varying complex gains were solved for using interleaved observations of the gain calibrator J0010 −4153, with an approximate scan length of 1.7 minutes every 21 minutes. Three 10 minute scans were carried out on the flux and bandpass calibrators approximately every 4 hr.

The data were reduced using OXKAT,[21] a semi-automated MeerKAT data analysis pipeline fully described in I. Heywood (2020) and I. Heywood et al. (2022), using a similar strategy to that described in S. C. Chapman et al. (2024). Briefly, the calibration strategy begins with cross-calibration, which includes frequency averaging to a channel width of 0.214 MHz, manual flagging of bad data and automated flagging of known and low-level radio frequency interference (RFI). Absolute flux calibration assumes J0408−6545 is a point source with Stokes I flux density of $S_\nu = 8.244$ Jy beam^{-1} with a spectral index of $\alpha = -1.138$ (where $S_\nu \propto \nu^\alpha$) at a reference frequency of 2406 MHz. Bandpass calibration also uses J 0408−6545 as a reference source, while

[21] https://github.com/IanHeywood/oxkat

Table 1
Radio-detected Sources at $z = 4.30$ in SPT2349−56

ID	R.A.	Decl.	S_{816} (μJy)	$S_{2.4}$ (μJy)	$S_{5.5}$ (μJy)	$S_{9.0}$ (μJy)	α	$L_{1.4,\mathrm{rest}}$ (10^{32} erg s^{-1} Hz^{-1})	P_{kin} $\times 10^{45}$ erg s^{-1}(f_{cav} 4^{-1})
A	23:49:42.68	−56:38:19.2	164 ± 24	71 ± 9	27 ± 5	11 ± 3	−1.02 ± 0.10	2.5 ± 0.3	0.27 ± 0.05
C	23:49:42.84	−56:38:25.1	718 ± 25	198 ± 9	60 ± 6	25 ± 4	−1.45 ± 0.08	20.1 ± 0.3	2.2 ± 0.1
E[a]	23:49:41.22	−56:38:24.6	76 ± 17	22 ± 7	<12	<13	−1.16 ± 0.29	1.0 ± 0.4	0.11 ± 0.04
N1	23:49:42.53	−56:37:33.2	69 ± 8	26 ± 5	<15	<19	−0.97 ± 0.18	0.7 ± 0.2	⋯
N2	23:49:43.54	−56:37:16.6	43 ± 8	20 ± 5	<17	<23	−0.74 ± 0.20	0.3 ± 0.1	⋯

Note. Five sources are individually detected by MeerKAT.
[a] For the 2.4 GHz measurement in *E*, the total flux extracted as discussed in Appendix A is 35 ± 12 μJy. Here, we conservatively measure the radio flux directly at the position of *E*. The 816 MHz flux is measured directly in the `robust=-2` image as shown in Figure B2. A residual 816 MHz flux measurement of 64 ± 11 μJy is also derived for *E* (after subtracting the bright source C) from the `robust=-1.2` image (shown in Figure 1).

time-variable complex gains are solved for using J 0010−4153 in eight spectral bins and a solution interval of 1.7 minutes. The solutions are then all transferred to the target visibilities. Apart from flagging, the cross-calibration process uses standard CASA tasks (J. P. McMullin et al. 2007) and is iterative, with each round applying updated data flags to improve RFI excision and the resultant calibration and image quality.

We employ a standard approach to self-calibration of MeerKAT data, where an initial deconvolution mask of the target field is created using a shallow unmasked clean, using a Briggs `robust` weighting[22] of −0.3. This mask is then used to create an initial sky model, which is iteratively improved along with the time-variable complex gain solutions through two rounds of antenna-based delay self-calibration using the CUBICAL package (J. S. Kenyon et al. 2018), splitting the data into eight spectral bins and time intervals of 64 s, with multi-frequency synthesis imaging performed during this process using WSCLEAN (A. R. Offringa et al. 2014). The primary beam's main lobe has a full width at half-maximum of 36′ at 2.4 GHz, well beyond the protocluster's few arcminute extent. We do not perform any direction-dependent calibration as the *S*-band residual image has a Gaussian-like noise distribution. As a final step, we use DDFACET (C. Tasse et al. 2023) to generate a 10,125 × 10,125 pixel image (pixel size = 0.″61, image area 1.7 × 1.7 deg^2) with Briggs `robust` weighting of 0 as a trade-off between desired angular resolution and achieved sensitivity. The resultant point-spread function FWHM dimensions are 4.″4 by 3.″4, at a position angle of -38.°8 east of north. The rms sensitivity in the vicinity of the target source of this final map is $\sigma = 4.3$ μJy beam^{-1}, and the effective frequency is 2.4 GHz, since the target is at the field center.

2.1.2. MeerKAT 816 MHz Data

The MeerKAT 816 MHz data processing and imaging were described in S. C. Chapman et al. (2024) and are not repeated here. The only difference is that the data were re-imaged with modified visibility weighting to better suit comparison with the new MeerKAT *S*-band data. While MeerKAT has baseline lengths that extend to 8 km, approximately 70% of its collecting area is concentrated within a central ∼1 km core. This results in a significant range of achieved sensitivity and angular resolution between uniform (`robust = -2`) and natural (`robust = +2`) imaging weightings. To facilitate comparison with the *S* band, we produce two UHF images to aid our analysis. We use a `robust = -2` weighting to maximize angular resolution (∼6″), while a second image with `robust = -1.2` (similar to S. C. Chapman et al. 2024) has degraded but still relatively high resolution (∼7″). A third `robust = -0.2` image provides higher sensitivity to probe the fainter, well-separated protocluster members in the north (see Figures 1 and A1).

2.2. ATCA Observations

SPT2349−56 was observed by the ATCA at 5.5 and 9.0 GHz from 2023 July 23 to 27 (PI: Aravena). We used the Compact Array Broadband Backend configured in the 1M-0.5k mode, which leads to a bandwidth of 2 GHz per correlator window with 1 MHz per channel of spectral resolution. The observations were performed in the most extended ATCA configuration, 6A, with six working 22 m antennas. The on-source time was 7.5 hr in each band.

The data were edited, calibrated, and imaged using the MIRIAD and CASA packages. Data affected by known RFI or with bad visibility ranges were flagged accordingly. We estimate an absolute calibration uncertainty of 5% at 5.5 GHz and 10% at 9.0 GHz. We inverted the visibilities using natural weighting, leading to beam sizes of 2.″7 × 1.″5 and 2.″1 × 1.″2 at 5.5 and 9.0 GHz, respectively, with associated rms noise values of 3.6 and 2.9 μJy beam^{-1}.

3. Results

Figure 1 shows the MeerKAT UHF 816 MHz imaging of the SPT2349−56 region from the new analysis presented in this work, highlighting the 110 mJy extended 870μm source (measured by the LABOCA camera on the APEX telescope), which defines the active protocluster region. The new *S*-band 2.4 GHz map (shown contoured over the UHF image) cleanly separates the radio emission from five known cluster sources: C, A, E, N1, and N2, where the two northern sources are also well detected individually in the UHF map. Fluxes are listed in Table 1.

Figure 1 also displays the ATCA 5.5 and 9 GHz maps, revealing two well-detected (17σ and 8σ) sources near the core of SPT2349−56 corresponding to Atacama Large Millimeter/submillimeter Array (ALMA) sources C and A. Both show signs of extension beyond the beam, with observed sizes derived from 2D Gaussian fitting of 4.″2 × 1.″6 (P.A. = 4.°7) and 3.″5 × 1.″6 (P.A. = 1.°1), respectively. Deconvolved from the beam, the true sizes are 3.″2 ± 1.″1 for C and 2.″2 ± 1.″3 for A in

[22] Briggs weighting is a compromise between uniform and natural weighting, parameterized by the robust parameter, typically between -1 (more uniform-like weights) and 1 (closer to natural weighting).

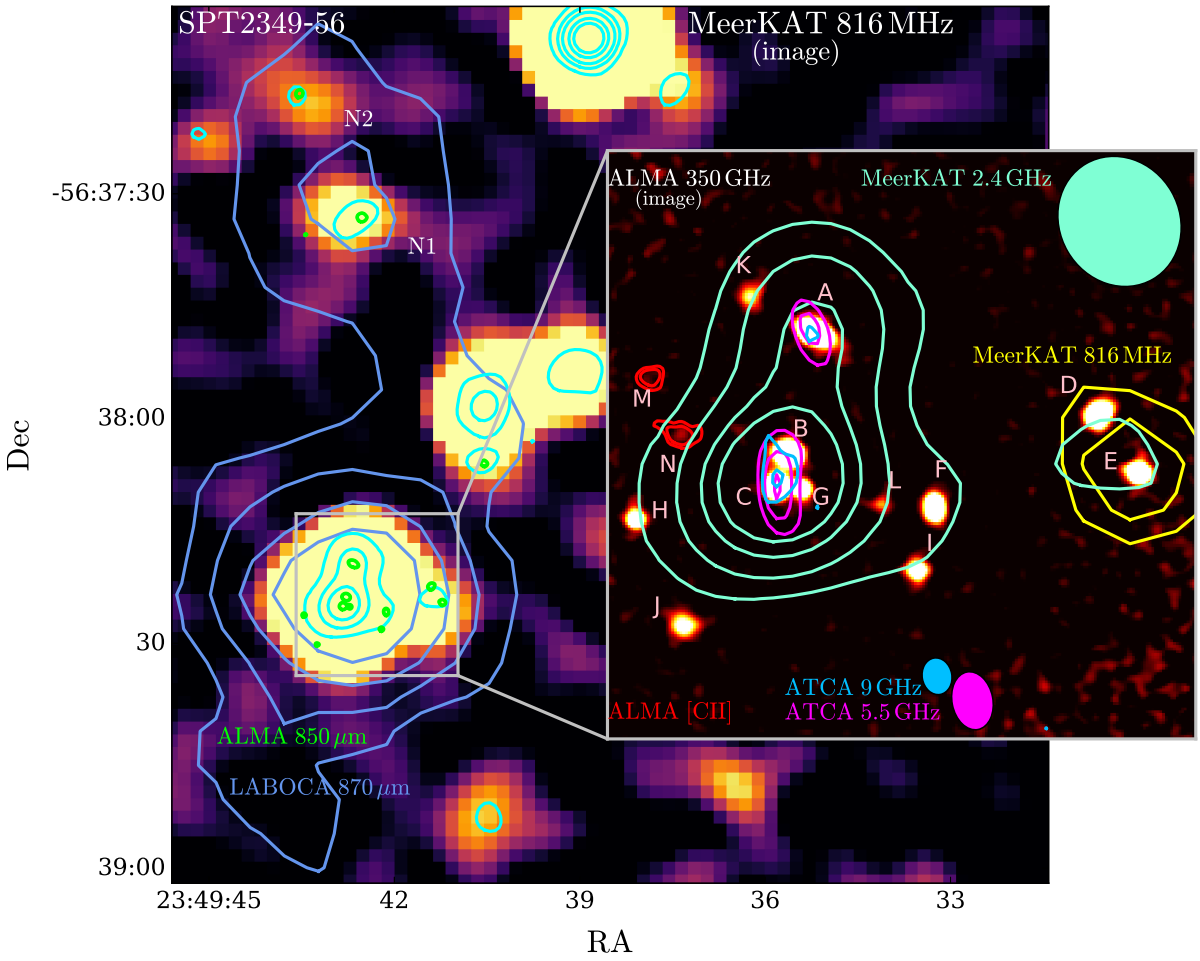

Figure 1. Background: MeerKAT 816 MHz `robust=-1.2` imaging of the SPT2349−56 region, with blue contours highlighting the 110 mJy extended LABOCA source at 870 μm (T. B. Miller et al. 2018), with ALMA 350 GHz sources shown (green contours). Inset: A 22″ × 22″ zoom-in of ALMA 350 GHz continuum imaging (R. Hill et al. 2020) with overlays of MeerKAT 2.4 GHz (cyan), ATCA 5.5 GHz (magenta) and 9 GHz (blue), beam shapes shown as filled ellipses. The point source removed UHF 816 MHz observation (highlighting source E) is shown as yellow contours. ALMA sources are named from T. B. Miller et al. (2018) in order of their 850 μm flux density. For the fainter ALMA sources M,N, we show [C II] contours (red).

roughly the north–south direction (and unresolved in the orthogonal direction). At 9 GHz, source C is unresolved while source A is only marginally detected. Sources E, N1, and N2, all undetected by ATCA, lie at 12″, 52″, and 69″ respectively from the phase center, resulting in attenuation of ∼25% for the northern sources at 5.5 GHz, and 50% at 9 GHz.

3.1. Source C: Revised Radio Power and Spectral Index

Source C was previously identified in S. C. Chapman et al. (2024) as the only radio source in SPT2349−56, with a radio luminosity sufficiently high as to be able to significantly heat any nascent ICM gas present in the core. With the new MeerKAT data, we are able to refine the analysis, noting that the radio luminosity for source C was previously overestimated by ≈10% (S. C. Chapman et al. 2024), as the blended radio emission with source A at ∼800 MHz from both MeerKAT and the Australian Square Kilometre Array Pathfinder was partially ascribed to C. Here we cleanly separate the emission from A and C using the 816 MHz MeerKAT data (Section 2.1.2) by reimaging with Briggs `robust=-2`, and deconvolving the emission with a double point source model (Appendix A). The revised MeerKAT 816 MHz flux, together with the three higher frequency bands, constrains a slope with high significance, $\alpha = -1.45 \pm 0.08$ (Figure 2), essentially unchanged from the previous estimate ($\alpha = -1.45 \pm 0.16$). We compute the rest-frame radio luminosity using the equation

$$L_{1.4} = (4\pi d_L^2\, S_{1.4}/10^{29})(1+z)^{-(\alpha+1)}\ \mathrm{erg\ s^{-1}\ Hz^{-1}}, \quad (1)$$

where d_L is the luminosity distance (in centimeters) and $S_{1.4}$ is the flux density in units of microjansky measured at 1.4 GHz, rest, with $S_\nu \propto \nu^\alpha$. At the SPT2349−56 redshift of 4.3, $L_{1.4}$ corresponds to an observed frequency of 264 MHz or wavelength of 214,287 μm as indicated in Figure 2. Source C accordingly has a revised 10% lower radio luminosity ($L_{1.4,\mathrm{rest}} = 2 \times 10^{33}$ erg s^{-1} Hz^{-1}). However, this still represents an excess of 125 times above the radio–far-infrared (FIR) relation at this frequency for relatively local star-forming galaxies (G. Helou et al. 1985), consistent with the high-z comparison of the relation shown in Figure 3. We note that recent studies (F. Gentile et al. 2025) have suggested the radio–FIR evolves (increases) mildly with increasing redshift (approximately 15% from $z = 0.5$ to 4.3, but dependent on where the division is drawn between star-forming galaxies and those with an AGN contribution). However, this result is not universally accepted, and we note that our assessment of the

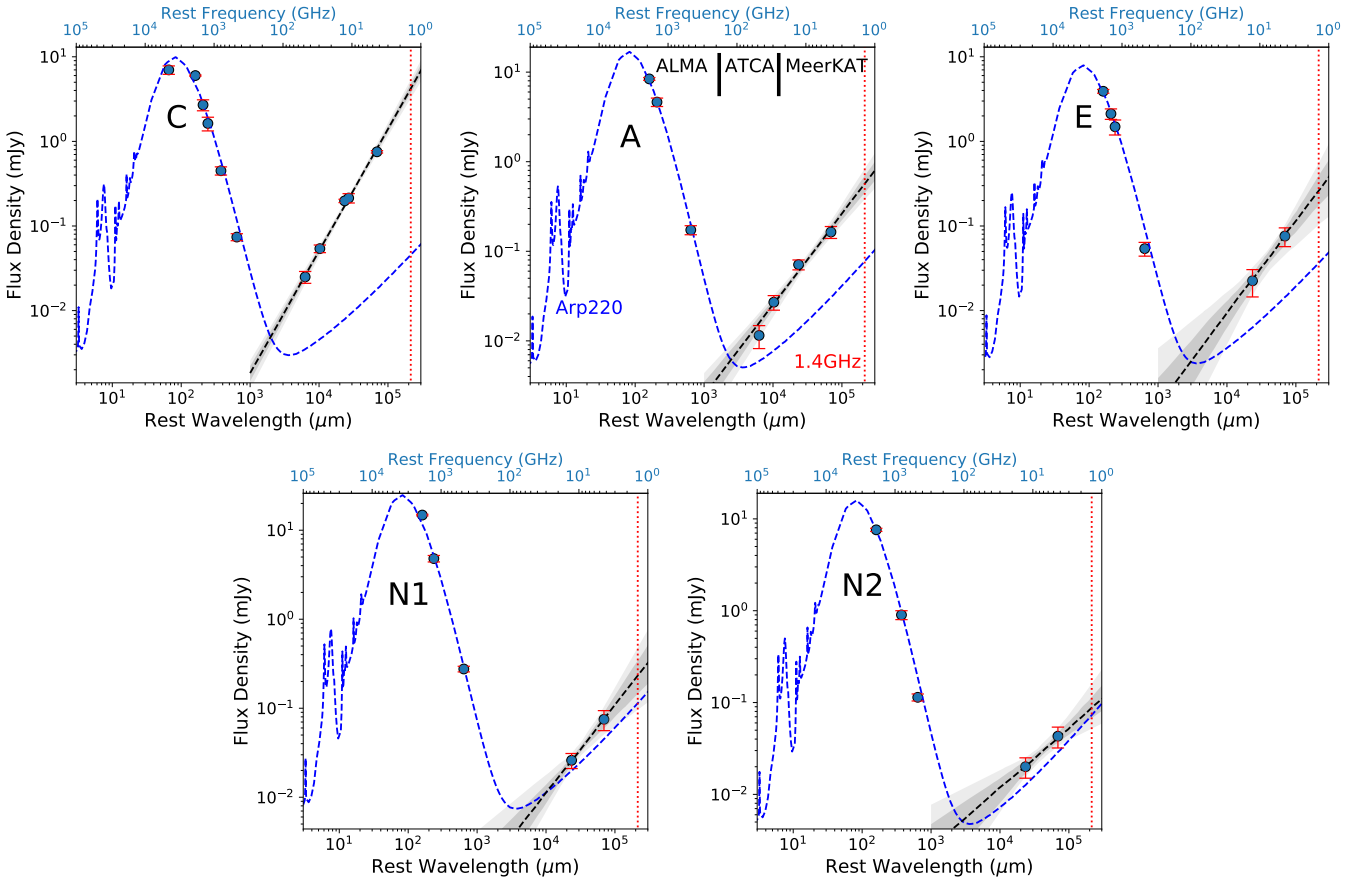

Figure 2. Spectral energy distributions (SEDs) for the five individually detected sources from MeerKAT. Also shown are the ALMA flux densities from R. Hill et al. (2020), and for 240 GHz from this work (Appendix B). For source C, a new 350 μm measurement from K. C. Harrington et al. (2025) is included, suggesting a slightly cooler SED than the $\sim$50 K found globally for the typically studied local ULIRG, Arp220 (C. D. Wilson et al. 2014). Arp220 lies near the mean of the local radio–FIR relation. Normalizing Arp220 to the submillimeter photometry reveals that three of the sources show significant excess in radio above the radio–FIR correlation for star-forming galaxies, while two (N1, N2) show no significant excess over that expected from star formation. Sources A and C are detected in the X-ray (F. Vito et al. 2024). The gray shadings show the 1σ and 2σ uncertainties in the radio spectral index fit (Appendix A). The red dash line indicates where $L_{1.4}$ is estimated for Figure 3 from Equation (1). Line labels and rest frequency ranges for data points from ALMA, ATCA, and MeerKAT are indicated on the source A panel.

GOODS-N radio and submillimeter galaxies shown in Figure 3 does not exhibit significant evidence for evolution in the relation from $z = 1$–4.

We also characterize the radio morphology at 5.5 GHz using the new high-resolution ATCA imaging, finding a significant extent centered about C of $3\farcs2 \pm 1\farcs1$, suggesting a projected bipolar radio jet is emanating from the AGN with a length of at least 22 kpc (see Section 4). This interpretation is strengthened by this candidate radio jet being oriented at 5° (east of north), almost perpendicular to the [C II] disk major axis, which lies at a P.A. = 125° (S. C. Chapman et al. 2024). The sensitivity of the ATCA 5.5 GHz imaging would only be able to detect the brightest parts of the jet (by analogy to lower-redshift and/or more powerful radio jets studied at high resolution), and the extent of the radio jets' influence on the cluster potential could be substantially larger. The extent of the jet is not significantly detected at 9 GHz despite the improved spatial resolution achieved over 5.5 GHz, the emission at 9 GHz is also well localized to ALMA source C. While the 5.5 GHz emission does extend partially over ALMA source B, the body of evidence above (along with C being an X-ray AGN) suggests this is indeed the radio jet from C projected over source B, rather than B contributing to the radio luminosity. Lower-level radio emission in B is expected from its FIR luminosity, but this would be a factor of $\sim$20$\times$ fainter than observed.

3.2. Two New Radio AGN in SPT2349−56

Four additional cluster members are individually detected by MeerKAT in the *S* band and the new UHF-band weightings (Section 2.1.2), namely, sources A and E from the original T. B. Miller et al. (2018) sample, along with sources N1 and N2 in the northern subgroup from R. Hill et al. (2020). The flux measurements are described in Appendix A. Sources A and E stand out at 816 MHz and 2.4 GHz as showing significant excess radio emission above the expectation from star formation alone, along with steep radio spectra characteristic of AGN (Figures 2 and 3). Their properties are summarized in Table 1, while Figure 3 compares these sources' radio luminosities and radio excess to literature samples of radio sources and SMGs. Radio-loud AGN are typically suggested as having $\sim$5$\times$ excess above the radio–FIR relation (e.g., E. Daddi et al. 2017; F. Gentile et al. 2025), which is easily satisfied by all of *C*, *A*, and *E* (Figure 3). While N1 does not exhibit radio excess, a possible AGN indication is present in its strong high-J CO emission (Appendix B), as well as its low [C II]/FIR ratio (R. Hill et al. 2020).

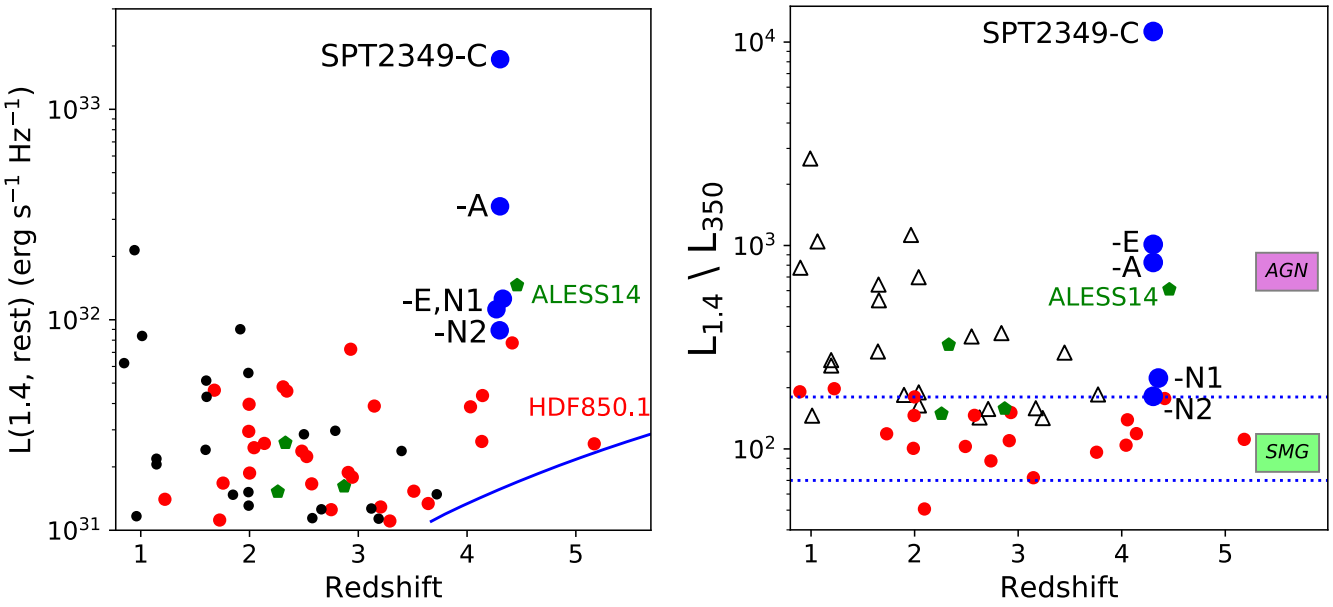

Figure 3. Left: redshift vs. 1.4 GHz radio power. Blue symbols represent SPT2349−56 radio detections (offset in redshift for clarity). We compare to the GOODS-N sample (A. J. Barger et al. 2017) (red circles show sources detected above the 3σ level at 850 μm, while black circles show sources not detected at this level), and the radio-excess candidates from the ALMA follow-up to the LABOCA ECDFS Submm Survey (ALESS) sample (A. P. Thomson et al. 2014) (green pentagons). SPT2349−56 source C has about 10 times more radio power than any radio source found in GOODS-N, while A, E, and N1 are among the top few percent in radio power found in GOODS-N. The blue line marks the radio flux limit in GOODS-N. Right: rest-frame 1.4 GHz luminosity over 350 GHz luminosity vs. redshift, with L_{350} derived using the Arp220 SED. Source C is about 125 times higher than the median relation at rest 1.4 GHz, with sources A and E being about 10 times higher. N1 and N2 do not appreciably distinguish themselves as expected. For comparison, we show the same submillimeter sources with spectroscopic redshifts in GOODS-N from the left panel (red circles), with lower limits on radio sources undetected in the submillimeter (black triangles). The blue dashed line region shows where the submillimeter luminosities and radio luminosities produce consistent estimates of SFRs. None of the GOODS-N SMGs show any significant excess radio emission over the FIR–radio relation.

Source A was previously identified as an X-ray-luminous AGN (F. Vito et al. 2024), and MeerKAT and ATCA observations reveal it to also be a relatively steep spectrum ($\alpha = -1.0 \pm 0.1$ on average) radio-loud AGN, with a radio excess of nine times above that implied by star formation. Its radio power is ≈8× lower than source C at 1.4 GHz (rest). Source A is detected with ATCA at 5.5 GHz and 9 GHz, and as with source C, shows evidence for some radio extent beyond the beam ($2\farcs2 \pm 1\farcs3$ or 15 kpc in length), possibly also implying jet emission. As with source C, this interpretation is strengthened by the somewhat opposing orientations of the jet (P.A. = 12°) and the [C II] disk (P.A. = 54°; A. Venkateshwaran et al. 2024), a difference which could even be interpreted as bipolar if the disk were sufficiently tilted into the line of sight. The radio spectrum is apparently much steeper at higher frequencies with ATCA than implied by MeerKAT at lower frequencies. This turnover may represent a very young radio source (Section 4.2). However, there is also a possibility that the radio source has a large spatial extent, and flux loss at higher frequencies may affect the spectral slope.

Source E is steeper in radio slope than A ($\alpha = -1.2 \pm 0.3$), although less well constrained as it is undetected at 5.5 GHz, and has more uncertainty in the MeerKAT fluxes (Appendix A). It represents a lower radio power source, but still with a radio excess of 9.4 times that inferred from its SFR.

The N1 and N2 sources are identified by MeerKAT as not having a significant radio excess over that expected from the radio–FIR correlation. However. N1 is also revealed to have a strong and compact ^{12}CO(11–10) line emission (Appendix B). N1 is the only source in SPT2349−56 showing a spectral line energy density (SLED) more like the AGN Mrk231 than the starburst galaxy M82. Source N1 is not detected in the X-ray (F. Vito et al. 2024), indicating either a deeply obscured Compton-thick AGN (the rest-frame optical counterpart shows very large extinction—R. Hill et al. 2022), or a modest mass SMBH below that expected from its stellar mass (R. Hill et al. 2022). Another explanation could be sub-Eddington accretion. N1 is an extremely luminous SMG, with an FIR luminosity over $3 \times 10^{13}\,L_\odot$ (R. Hill et al. 2020; D. Zhou et al. 2025), with an implied SFR of almost $3000\,M_\odot$ yr^{-1}. As such, the copious radio emission associated with its SFR could dominate over a weaker radio-AGN component.

3.3. Radio Contribution from Star Formation

Sources N1 and N2 are the most FIR-luminous sources in the cluster, with N2 being comparable to the brightest source A in the core region. Both are individually detected in the MeerKAT UHF and the *S* band (Table 1), revealing the radio emission and synchrotron slope ($\alpha \sim -0.8$) expected from the correlation with FIR luminosity (Figure 2). While both sources exhibit a small excess above the median in the local radio–FIR relation, it is consistent within 2σ of the radio photometry errors and uncertainties in the slope α (Appendix A.2), and well within the 0.2 dex scatter in the local relation. As such, there is no strong evidence in SPT2349−56 sources for an increase in radio–FIR sometimes claimed at high redshifts (e.g., F. Gentile et al. 2025).

The detections of N1 and N2 suggest that marginally significant radio emission from some of the other brighter cluster members may be blended with the central radio AGN, as hinted at in the *S*-band image in Figure 1. In the residual map of the core at the *S* band, after subtracting sources C, A, and E, there is a marginal excess in radio emission revealed in the region of sources F and D, which would be consistent with

that expected ($\sim$5 μJy) from the radio–FIR relation. The residual emission does not, however, represent even a $>3\sigma$ detection.

4. Discussion

4.1. Overdensity of Radio AGN

Three radio AGN in this small $z = 4.3$ core volume (the central 19″ or 130 kpc diameter) is an enormous overdensity, 130,000 deg^{-2}. When considered as a spherical volume, this is a factor of $>10^7\times$ larger than found in deep radio surveys followed up spectroscopically, like that in the Great Observatories Origins Deep Survey North (GOODS-N; A. J. Barger et al. 2007) or COSMOS (V. Smolčić et al. 2017). Comparing the recent characterization of radio-excess galaxies in COSMOS (F. Gentile et al. 2025), considering the $z = 3$–5 range, between six and 11 radio sources are found in the 0.54 deg^2 JWST field (11–20 deg^{-2}) with at least the level of radio excess found in our three SPT2349−56 radio AGN. This translates into $\sim$15 radio AGN in 9.6×10^4 Mpc^{-3} (physical distances) compared to SPT2349−56 with 2600 radio AGN Mpc^{-3}—an overdensity of 1.66×10^7.

When we consider that radio AGN typically represent only $\approx$10% of the total AGN population (F. Panessa et al. 2019), our finding would naively suggest that there could be substantially more radio-quiet AGN in the SPT2349−56 core. In fact, these three central radio AGN represent all of the AGN currently known in the core region.

There are $\sim$40 cluster members in the protocluster identified to date, the vast majority selected by submillimeter continuum or [C II] line emission (N. Sulzenauer et al. 2025), and further observations (e.g., with JWST) may identify other galaxies as hosting lower-luminosity (radio-quiet) AGN. Four AGN among the $\sim$30 submillimeter-emitting cluster members now cataloged is not particularly unusual, representing a fairly typical 13% AGN fraction for protoclusters, although these numbers are sensitive to depths of surveys at different wavelengths. If we consider only the 14 ultra-luminous infrared galaxies (ULIRGs) in SPT2349−56 with an SFR $> 100\,M_\odot$ yr^{-1}, the AGN fraction is 29%.

Other claimed multiple radio AGN in protoclusters, such as the two identified by E. Daddi et al. (2017) in the $z = 2.5$ Cl J1001, would not come close to being classified as radio-loud AGN by our criteria (as shown in Figure 3), with radio luminosities only $\approx 5 \times 10^{31}$ erg s^{-1} Hz^{-1} at 1.4 GHz, rest, and modest excess over the radio–FIR expectation. Even the closest known analog to SPT2349−56 in the dense DRC protocluster (I. Oteo et al. 2018) shows only a single radio AGN, along with two X-ray identified AGN (F. Vito et al. 2020). Finding a single radio AGN is typical in general of many protocluster fields, some of which are actually selected using the radio AGN itself—e.g., the Spiderweb (H. Dannerbauer et al. 2014). This basic finding is possibly related to a key aspect of galaxy cluster evolution, that radio jets are thought to provide an important feedback mode in galaxy clusters by preventing the cooling of hot (X-ray) gas surrounding central galaxies (B. R. McNamara & P. E. J. Nulsen 2012).

4.2. Energetics of the Radio AGN

Simple energetic considerations establish that radio jets can, in principle, have drastic effects on the gas-phase baryons in and surrounding massive galaxies. D. Zhou et al. (2026) have argued that in SPT2349−56, the large overdensity of radio AGN discovered in this work represents an energetically favorable way to explain the energy input into the ICM that may drive the large SZ signal they observe. D. Zhou et al. (2026) showed that neither shocks from gravitational contraction nor supernovae from star formation could supply the observed heating of the ICM. For AGN outflows and radiative heating from the AGN itself, we have calculated in D. Zhou et al. (2026) that this also cannot easily produce the required excess thermal reservoir. A. Sokołowska et al. (2018) find that the early circumgalactic medium (CGM) is established through hot outflows directly from the central galaxy driven by supernova feedback, rather than infalling gas which is shock heated or heated by feedback (although they focused on a Milky Way–like galaxy and did not include AGN). While this is an interesting hypothesis to consider for AGN in SPT2349−56, there would not be nearly enough gas mass expelled from these three central AGN to account for the thermal Sunyaev–Zel'dovich (tSZ) decrement, unless the temperature were unreasonably high. Extended Data Figure 8 in D. Zhou et al. 2026 would suggest $>10^8$ K even with all the present gas mass in galaxies A, C, and E ($M_{\rm H2} = 1.3 \times 1011\,M_\odot$ in R. Hill et al. 2020) being expelled in a hot outflow.

The total energetic output from the three radio AGN described herein ($L_{1.4} = 2.6 \times 10^{26}$ W Hz^{-1}) is not significantly larger than the previous (overestimated) radio luminosity (2.2×10^{26} W Hz^{-1}) presented for the single central AGN (S. C. Chapman et al. 2024). However, the fact that three likely randomly oriented radio jets are impacting the ICM may facilitate seeing such an early, large, and uniform tSZ decrement aligned with the protocluster center of mass (S. Cielo et al. 2018). This contrasts all other protocluster tSZ detections found at $z \sim 2$, where large spatial offsets are observed between the SZ decrement and the core region of the cluster (A. B. Mantz et al. 2018; R. Gobat et al. 2019; L. Di Mascolo et al. 2023).

S. C. Chapman et al. (2024) speculated that the radio AGN in SPT2349−56 can be fueled by hot gas in radio mode instead of radiative-efficient accretion through recent mergers, which can provide strong kinetic feedback with substantial energy injection on the nascent ICM in the protocluster. The two modes of accretion (radio or quasar mode) are in fact somewhat oversimplified, and various studies have found that radio jets can be more complicated. One example is studied in P. N. Best & T. M. Heckman (2012) with two distinct radio-AGN populations: (1) low-excitation radio AGN and (2) high-excitation radio AGN. The latter (category 2) does not require the inefficient accretion that is thought to be important for radio AGN defined more broadly. Especially since we now identify radio-excess galaxies spanning a $>10\times$ range in radio power, the initial suppositions from S. C. Chapman et al. (2024) may be less applicable for the lower-luminosity radio AGN in galaxies A and E.

We first use the locally characterized correlation between the cavity power ($P_{\rm cav}$) and radio luminosity (C. J. Willott et al. 1999) at 1.4 GHz ($L_{1.4\,\rm GHz}$) to estimate a kinetic power from radio luminosity alone for each of the radio AGN (listed in Table 1), which is adopted over a large range in redshifts as in K. W. Cavagnolo et al. (2010) and T. M. Heckman & P. N. Best (2014):

$$P_{\rm cav} = 7 \times 10^{43}\ {\rm erg\ s^{-1}} \times f_{\rm cav} \left(\frac{L_{1.4\,\rm GHz}}{10^{25} {\rm W\ Hz^{-1}}} \right)^{0.68}, \qquad (2)$$

where the enthalpy factor $f_{\rm cav} = 4$ for relativistic plasma. Shocks induced by the radio jet can cause additional heating, which could imply a higher $f_{\rm cav} > 4$ (A. Nusser et al. 2006). This scaling relation yields a total kinetic power from the three radio AGN of $\dot{E}_{\rm kin,radio} = (2.6 \pm 0.3) \times 10^{45}\,{\rm erg\,s^{-1}} \times (f_{\rm cav}/4)$.

Assuming $f_{\rm cav} = 4$, we can estimate the energy input as

$$\Delta E_{\rm inject} \approx \dot{E}_{\rm kin,radio} t_{\rm radio} = \left[(8.7 \pm 0.8) \times \left(\frac{t_{\rm radio}}{100\,{\rm Myr}}\right)\right] \times 10^{60}\,{\rm erg}. \quad (3)$$

Adopting a typical $t_{\rm AGN} = 100$ Myr (M. Brienza et al. 2017) for AGN activity, we obtain a total energy injection of $(8.7 \pm 0.8) \times 10^{60}$ erg to be stored in the nascent ICM, comparable to that estimated directly from the tSZ decrement ($\sim 10^{61}$ erg) in D. Zhou et al. (2026). We note that radio-AGN lifetimes are characterized as long as $t_{\rm AGN} = 500$ Myr, but are generally characterized between 50 and 100 Myr (M. J. Hardcastle et al. 2019). Thus, there is considerable uncertainty in our use of $t_{\rm AGN}$ in this equation. In this "high-temperature (feedback)" scenario, powerful energy injection from the known radio AGN has superheated the gas (S. C. Chapman et al. 2024; D. Zhou et al. 2026), creating the tSZ signal through a modest ICM gas mass heated to high temperatures ($>3 \times 10^7$ K). However, the strong tSZ signal requires a nearly 100% coupling efficiency if the energy is solely provided by the identified radio-loud AGNs. The energetic jets may not couple efficiently to the bulk of the ICM gas (A. Babul et al. 2013; H. Y. K. Yang & C. S. Reynolds 2016; S. Cielo et al. 2018). This scenario is, however, testable—this same feedback would also suppress the X-ray luminosity expected from the ICM compared to that generated by gravitational energy (e.g., accretion shocks; X. Shi 2016) from a massive halo. Such a low-mass ICM heated to a higher temperature will puff up the gas and lead to X-ray cavities (J. Rasmussen & T. J. Ponman 2009), which do not increase the X-ray photons. However, the X-ray spectrum substantially shifts to higher energy, which could be detectable in the X-ray by XMM-Newton, for example.

4.3. Synchronizing Three Radio AGN

A key question is how the three radio AGN in the core of SPT2349−56 can be simultaneously active in this small volume. Y. Li et al. (2008) provide a simplified model of jet power from AGN, whereby disk accretion is combined with the sum of two mechanisms of extracting energy magnetically from a black hole accretion disk, i.e., the Blandford–Payne (BP; R. D. Blandford & D. G. Payne 1982) and the Blandford-Znajek (BZ; R. D. Blandford & R. L. Znajek 1977) processes. In the BP process, the disk matter streams into the outflow/jet by way of the poloidal magnetic field lines frozen in the disk. The channeled gas is then accelerated via work done by the magnetic torque. The BZ process, although not physically viable on its own (B. Punsly 2001) provides an approach used in Y. Li et al. (2008) to explain why some AGN are intensely bright in radio waves (radio-loud) while others are not (radio-quiet). Rapidly spinning SMBHs with sufficient magnetic fields are more likely to produce powerful jets. As the black hole rotates, the magnetic field lines, which are frozen into the plasma of the accretion disk, are twisted and stretched, converting the black hole's rotational energy into electromagnetic energy. This extracted energy is then channeled along the twisted magnetic field lines and flung outwards as a highly collimated beam of ionized matter, resulting in a relativistic jet. There are possible mechanisms to keep radio galaxies active longer than ∼100 Myr (M. Brienza et al. 2017), but arguing for these exceptional circumstances happening on the scale of the central SMBHs is contrived, even in the overdense environment of SPT2349−56.

A more plausible explanation is simply that the mega-merger (D. Rennehan et al. 2020) resulting from the remarkably overdense core environment (more than any ever identified in the Universe) may have driven AGN into a radio mode. The mega-merger nomenclature in D. Rennehan et al. (2020) refers to a complete merger of all 14 massive galaxies in the SPT2349−56 core within a few hundred Myr timescale. The core environment is overdense in galaxies by any metric (stars, SFR, or gas) as well as radio AGN, but is not so obviously elevated in AGN fraction compared to the field (as above). Gravitational interaction is significantly increased in the system, which could enhance the cold gas accretion to AGN for a more efficient accumulation of spin (powering the radio jets). The possible importance of merger-induced radio AGN is described in T. M. Heckman et al. (2024), a mechanism that suggests that all the luminous AGN may have therefore become radio-loud through galaxy interactions within the expected ≈100 Myr timescale found for radio activity (M. J. Hardcastle et al. 2019). Further, S. Cielo et al. (2018) have studied precessing radio jets in an ICM, with implications that the interaction of the jets and random orientations may actually be important for ICM heating. More detailed studies of the SPT2349−56 radio AGN are warranted.

4.4. Radio Source Properties and Lifetimes

Two new pieces of information have emerged from our updated study: resolved jet sizes and steep spectral indices (α) confirmed at higher frequencies (>5 GHz). A steep spectrum is typically derived from self-absorbed synchrotron, along with a lack of electron injection (e.g., J. F. Radcliffe et al. 2021). Thus, the steep α measured in these three radio AGN could represent a dying radio source. On the other hand, these properties could be explained as due to a confined or "frustrated" radio source inside a dense medium, still building in radio power. This would be consistent with the observed hot ICM in D. Zhou et al. (2026). These confined radio sources are sometimes referred to as compact steep spectrum (CSS) sources (P. Padovani 2017). However, the luminosities of the SPT2349−56 radio sources are low relative to typical GHz-peaked CSS sources, even in the case of source C. While the three radio AGN in SPT2349−56 span a factor of ∼20 in $L_{1.4}$, it is possible that they may have had a more equal or different distribution in radio power in the recent past, since it is unclear what the history or lifetime of any of the three is. If a self-absorbed synchrotron is contributing to the steep spectrum, the observational constraints would mean that the break frequency is below about 5 GHz in the rest frame (940 MHz in observed). This break frequency (as seen explicitly in source A) can provide a constraint on the age of the radio source. However, if the radio emission is due to a CSS then it would have to be older than 500 Myr to have a break frequency below 900 MHz rest (4.8 GHz observed) (P. Padovani 2017).

5. Conclusions

We have used new MeerKAT radio observations to find two additional radio-excess galaxies (*A* and *E*) in SPT2349−56 (both ∼10× above the radio–FIR correlation at 1.4 GHz), for a total of three radio AGN in the cluster, including the previously identified source C. Two of these AGN (A and C) are also X-ray detected (F. Vito et al. 2024). One other candidate AGN (source N1) is detected in the radio, but does not show an obvious excess over that expected from star formation. The AGN in N1 is only identified through an excess in CO(11–10) emission (comparable to Mrk231), indicating a flat CO SLED to at least $J = 11$. The lack of enhanced radio or X-ray emission indicates that it is Compton thick and radio-quiet.

1. Four AGN among the ∼30 submillimeter-emitting cluster members now cataloged (N. Sulzenauer et al. 2025) represent a fairly typical 13% AGN fraction for $z > 2$ protoclusters, although this fraction goes up to 29% considering only the 14 ULIRGs.
2. However, the overdensity of three radio AGN in SPT2349−56 is within a 130 kpc diameter region, which is larger than has been previously documented in the literature, where no more than one radio AGN has ever been reported in a central (proto-)cluster region (e.g., C. M. Casey et al. 2015; I. Oteo et al. 2018; P. Tozzi et al. 2022). However, the statistical uncertainty of three versus one is small. For reference, the field density of similar radio-excess galaxies in COSMOS is 1.66×10^7 times lower at $z = 3$–5.
3. The three central radio AGN are likely heating the nascent ICM, providing an estimated power of $(2.6 \pm 0.3) \times 10^{45}\,\mathrm{erg\,s^{-1}} \times (f_{\rm cav}/4)$, and could give rise to the abnormally large tSZ signal detected in D. Zhou et al. (2026). The interaction of the jets and random orientations may be important for ICM heating, e.g., S. Cielo et al. 2018.
4. The direct evidence for compact radio jets from the 5.5 GHz morphology, and the more tentative evidence for a spectral break below ∼5 GHz (in source A) argue for young radio sources and/or confined medium, again supporting an interaction with the hot ICM detected in this system.

Acknowledgments

We thank Renyue Cen and Daisuke Nagai for the very useful conversations that helped shape the discussion in this Letter. We thank an anonymous referee for the thoughtful and constructive report, which has significantly improved the Letter.

The MeerKAT telescope is operated by the South African Radio Astronomy Observatory, which is a facility of the National Research Foundation, an agency of the Department of Science and Innovation. The research of RPD is supported by the South African Research Chairs Initiative (grant ID 77948) of the Department of Science and Innovation and the National Research Foundation. The Australia Telescope Compact Array is part of the Australia Telescope National Facility (https://ror.org/05qajvd42), which is funded by the Australian Government for operation as a National Facility managed by CSIRO. The National Radio Astronomy Observatory is a facility of the National Science Foundation operated under cooperative agreement by Associated Universities, Inc. This Letter makes use of the following ALMA data: ADS/JAO.ALMA#2021.1.01313.S, ADS/JAO.ALMA#2018.1.00058.S, and ADS/JAO.ALMA#2021.1.01010.P. ALMA is a partnership of ESO (representing its member states), NSF (USA) and NINS (Japan), together with NRC (Canada), MOST and ASIAA (Taiwan), and KASI (Republic of Korea), in cooperation with the Republic of Chile. The Joint ALMA Observatory is operated by ESO, AUI/NRAO, and NAOJ. S. C.C., D.Z., J.B., C.H., R.H., V.P., and G.W. gratefully acknowledge support for this research from NSERC. This research was supported in part by grant No. NSF PHY-2309135 to the Kavli Institute for Theoretical Physics (KITP). Manuel A. acknowledges support from FONDECYT grant 1211951, CONICYT + PCI + INSTITUTO MAX PLANCK DE ASTRONOMIA MPG190030.

Appendix A
Analysis of the MeerKAT Data

A.1. Radio Flux Measurements

The MeerKAT images used for flux measurements in Table 1 are shown in Figure A1. Five source positions (A, C, E, N1, and N2) were modeled as unresolved sources in both *S*-band and UHF imaging, with peak positions allowed to vary. Subtracting these five sources yields residuals $<2\sigma$ as shown. The source positions do not vary by more than 1.″5 from the ALMA centroid in each case (i.e., well within the MeerKAT positional uncertainty, given the angular resolution and signal-to-noise ratio (SNR) of these detections).

In the `robust=-1.2` UHF 816 MHz map, the central C, A, and E regions are blended (Figure 1); however, in the `robust=-2` weighting, source E is cleanly separated, allowing a straightforward flux measurement (Table 1). An additional estimate of the UHF flux density for E was made using the more sensitive `robust=-1.2` UHF map. Point source subtraction was performed on the UHF central region, removing the strong emission associated with ALMA source C. This map results in the identification of a strong 816 MHz emission (6.3σ) centered on-source E, shown in Figure 1. There remains a possibility that the neighboring source D ($S_{850} = 4.5$ mJy) has radio emission roughly consistent with its SFR (expected to be 7 μJy at 2.4 GHz; 15 μJy at 816 MHz), and that source E is somewhat less radio-loud (7× compared to the 9.4× excess inferred if all the measured UHF radio flux is coming from E).

For the source E, while the higher SNR `robust=-1.2` UHF source extraction lies 0.″4 from the ALMA centroid, the *S*-band source extraction lies midway to the neighboring source D (Figure A1). Source D lies 3″ away from E, and the *S*-band source extraction centroid lies approximately 40% toward D (1.″2 offset from E). Since D is expected to have ∼7 μJy *S*-band flux based on its FIR luminosity, we instead extract peak *S*-band flux positions at the ALMA positions of sources E and D, finding 21 ± 5 μJy at E and 12 ± 5 μJy at D. The sum is consistent with the 35μJy peak source subtraction above.

A.2. Radio Spectral Indices

We derive radio spectral indices directly for all five radio-detected SPT2349−56 sources and list these in Table 1. The

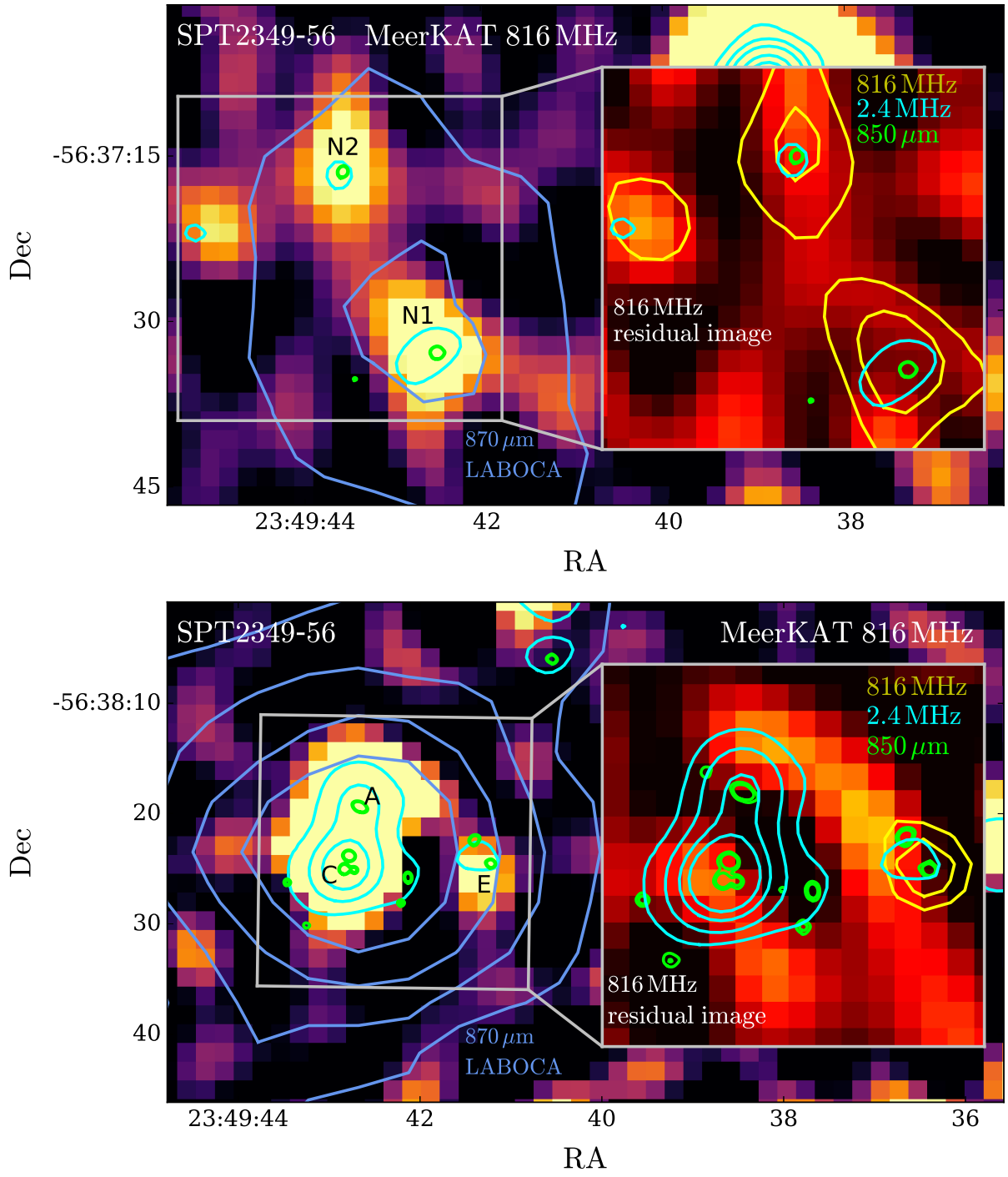

Figure A1. Zoomed in MeerKAT UHF maps with *S*-band contours (cyan) overlaid and radio sources labeled. The `robust=-0.2` map is used for the north (TOP panel) to maximize sensitivity to the well-separated N1 and N2 sources. The highest resolution weighting `robust=-2` is used for the core (bottom panel) to cleanly separate source E from A and E. The protocluster region is highlighted by 870 μm APEX-LABOCA contours (blue). Insets: residual maps of the MeerKAT UHF images are shown, after subtracting the five SPT2349−56 sources: A, C, E, N1, N2. Protocluster sources detected by ALMA are identified with green contours in both the MeerKAT image and residual image. The MeerKAT maps are contoured over the residual maps for UHF (yellow) and the *S* band (cyan). For the core region (lower panel), we show in yellow contours only the residual "source C-subtracted" UHF map (`robust=-1.2`), which exhibits the highest SNR, 6.4σ detection of source E.

data were fit according to a linear function in log-space using a Markov Chain Monte Carlo (MCMC) algorithm implemented by the `emcee` package (D. Foreman-Mackey et al. 2013). This MCMC package samples the posterior probability function and is used to determine the error contours shown in Figure 2, as well as the uncertainties on α in Table 1.

Appendix B
CO SLED Analysis of SPT2349−56 Members

B.1. New ALMA Observations

Extensive ALMA properties of these radio-detected SPT2349−56 sources (A, C, E, N1, N2) have already been published (T. B. Miller et al. 2018; R. Hill et al. 2020;

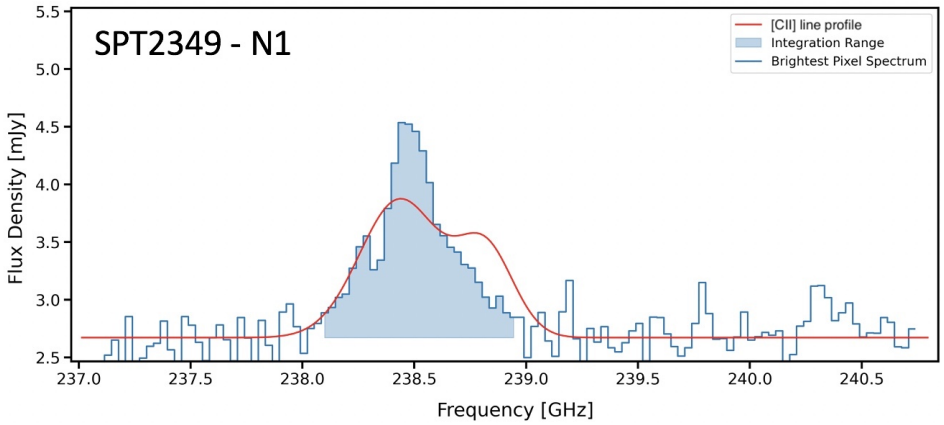

Figure B1. CO $J_{\rm upper} = 11$ spectrum of N1, significantly brighter than any other in the protocluster, and much narrower than the CO(4–3) and [C II] lines. Analysis of the CO SLED (below) suggests a possible AGN-driven contribution to the gas excitation (Figure B2). The red line denotes the aperture-integrated [C II] spectrum of N1.

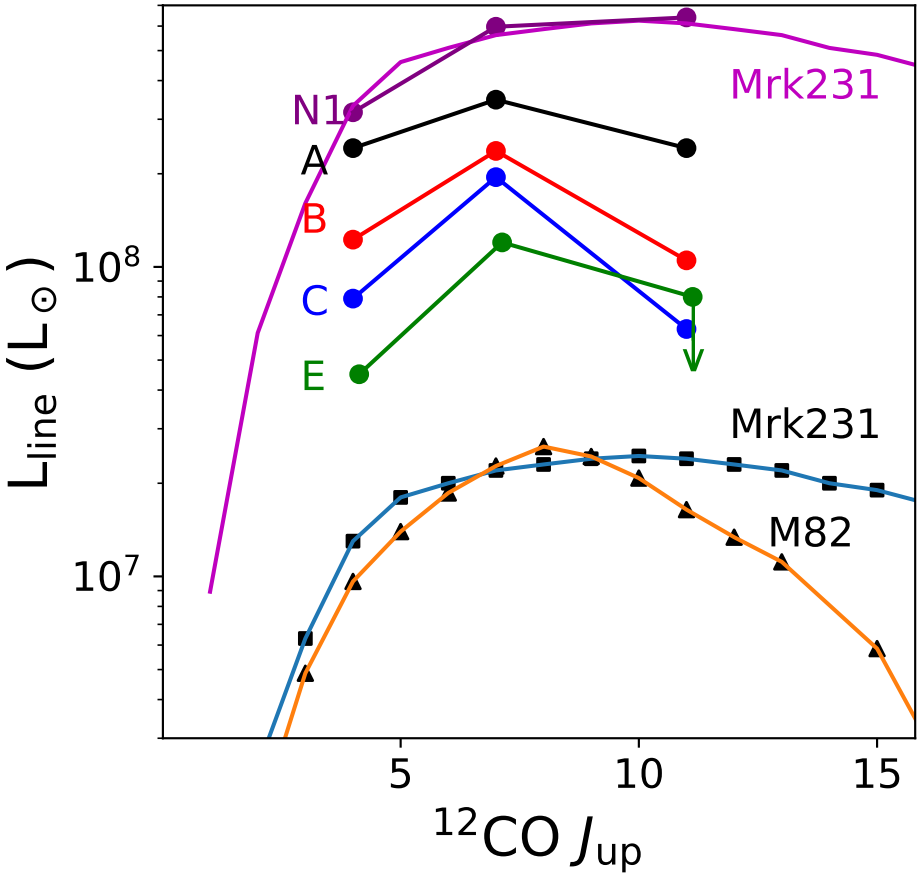

Figure B2. SLEDs for the sources detected at $>5\sigma$ in the CO $J_{\rm upper} = 11$ transition. New spectral data for the $J_{\rm upper} = 11$ lines are shown in Figure B1. We compare to the $L_{\rm FIR} = 3 \times 10^{12}\,L_\odot$ AGN-dominated galaxy Mrk231 (P. P. van der Werf et al. 2010), and the $L_{\rm FIR} = 3 \times 10^{10}\,L_\odot$ starburst M82 (J. Kamenetzky et al. 2012), here normalized to Mrk231 at CO(7–6). Source N1 shows an excess $J = 11$ emission at very high significance, with almost perfect agreement with the Mrk231 SLED modeled with a strong XDR (see the text) contribution (P. P. van der Werf et al. 2010). The radio AGN A and C show SLEDs more consistent with starburst galaxies. The radio AGN *E* is not significantly detected in CO(11–10), but we show it here as it is also consistent with an M82-like excitation (plotted as 3σ).

K. M. Rotermund et al. 2021; S. C. Chapman et al. 2024; C. Hughes et al. 2025). Here we present new ALMA observations (Table B1), supporting our measurements of line emission in the context of searching for AGN.

The Cycle 8 program (2021.1.01313.S, PI: Canning), described initially in S. C. Chapman et al. (2024) for sources B, C, and G, observed ^{12}CO(11–10) ($\nu_{\rm rest} = 1267.01$ GHz) and continuum at about 240 GHz in Band 6. These observations, carried out on 2022, September 1, used the C-4 array configuration with baselines of 15–784 m, giving a naturally weighted synthesized beam size of $0\farcs47$. J2357−5311 and J2258−2758 were used to calibrate the amplitude, while J2357−5311 and J2336−5236 were used to calibrate the phase. All the data were calibrated using the standard observatory-supplied calibration script. Imaging was done using the CASA task `tclean`, using Briggs weighting with a robust parameter of

Table B1
CO(11–10) Measurements and Associated 240 GHz Continuum in the SPT2349−56 Galaxies with Significant (>5σ) Detections

ID	R.A.	Decl.	S_{240} (mJy)	$S_{CO(11-10)}$ (Jy km s^{-1})	$L_{CO(11-10)}$ (10^8 $L_\odot$)
A	23:49:42.68	−56:38:19.2	2.8 ± 0.3	0.37 ± 0.06	24.2 ± 4.4
B	23:49:42.78	−56:38:23.8	2.2 ± 0.2	0.20 ± 0.03	10.6 ± 2.1
C	23:49:42.84	−56:38:25.1	1.9 ± 0.2	0.18 ± 0.03	6.3 ± 1.2
N1	23:49:42.53	−56:37:33.2	4.8 ± 0.2	0.98 ± 0.08	64.0 ± 4.9

0.5, and in all cases, channel widths were averaged down to a common 15.625 MHz.

Reduction and analysis followed the same procedures described in C. Hughes et al. (2025). The same apertures used by R. Hill et al. (2020) to extract line and continuum measurements were applied to all sources in order to extract one-dimensional CO(11–10) spectra for each source. New continuum flux densities and line strengths are listed in Table B1, updating sources previously presented in (S. C. Chapman et al. 2024), and the new continuum measurements are also shown in Figure 2. Source N1 (spectrum shown in Figure B1) distinguishes itself from other sources in the protocluster with a flat SLED (Figure B2), typically requiring X-ray dominated regions (XDRs) to explain the excess, as in the local AGN Mrk231 (P. P. van der Werf et al. 2010). XDRs are areas of interstellar gas where high-energy X-ray photons (typically $E > 1$ keV) are the primary drivers of the chemistry and heating, rather than the far-ultraviolet photons that dominate photon-dominated regions. None of the radio AGN show signs of XDR contributions to their ^{12}CO SLED.

ORCID iDs

Scott C. Chapman https://orcid.org/0000-0002-8487-3153
Roger P. Deane https://orcid.org/0000-0003-1027-5043
Dazhi Zhou https://orcid.org/0000-0002-6922-469X
Manuel Aravena https://orcid.org/0000-0002-6290-3198
Melanie Archipley https://orcid.org/0000-0002-0517-9842
Jared Cathey https://orcid.org/0000-0002-4657-7679
Anthony H. Gonzalez https://orcid.org/0000-0002-0933-8601
Ryley Hill https://orcid.org/0009-0008-8718-0644
Mònica Natalia Isla Llave https://orcid.org/0009-0004-4516-0558
Matt Malkan https://orcid.org/0000-0001-6919-1237
Kedar A. Phadke https://orcid.org/0000-0001-7946-557X
Vismaya Pillai https://orcid.org/0009-0003-6250-1396
Bonnie Slocombe https://orcid.org/0009-0008-7012-2077
Manuel Solimano https://orcid.org/0000-0001-6629-0379
Justin Spilker https://orcid.org/0000-0003-3256-5615
Nikolaus Sulzenauer https://orcid.org/0000-0002-3187-1648
Fabio Vito https://orcid.org/0000-0003-0680-9305
Joaquin D. Vieira https://orcid.org/0000-0001-7192-3871
George Wang https://orcid.org/0009-0003-4626-9777
Axel Weiss https://orcid.org/0000-0003-4678-3939

References

Babul, A., Sharma, P., & Reynolds, C. S. 2013, ApJ, 768, 11
Barger, A. J., Cowie, L. L., Owen, F. N., Hsu, L. Y., & Wang, W. H. 2017, ApJ, 835, 95
Barger, A. J., Cowie, L. L., & Wang, W. H. 2007, ApJ, 654, 764
Best, P. N., & Heckman, T. M. 2012, MNRAS, 421, 1569
Blandford, R. D., & Payne, D. G. 1982, MNRAS, 199, 883
Blandford, R. D., & Znajek, R. L. 1977, MNRAS, 179, 433
Brienza, M., Godfrey, L., Morganti, R., et al. 2017, A&A, 606, A98
Brodwin, M., Stanford, S. A., Gonzalez, A. H., et al. 2013, ApJ, 779, 138
Casey, C. M., Cooray, A., Capak, P., et al. 2015, ApJL, 808, L33
Cavagnolo, K. W., McNamara, B. R., Nulsen, P. E. J., et al. 2010, ApJ, 720, 1066
Chapman, S. C., Blain, A., Ibata, R., et al. 2009, ApJ, 691, 560
Chapman, S. C., Hill, R., Aravena, M., et al. 2024, ApJ, 961, 120
Cielo, S., Babul, A., Antonuccio-Delogu, V., Silk, J., & Volonteri, M. 2018, arXiv:1801.04276
Daddi, E., Jin, S., Strazzullo, V., et al. 2017, ApJL, 846, L31
Dannerbauer, H., Kurk, J. D., De Breuck, C., et al. 2014, A&A, 570, A55
Di Mascolo, L., Saro, A., Mroczkowski, T., et al. 2023, Natur, 615, 809
Digby-North, J. A., Nandra, K., Laird, E. S., et al. 2010, MNRAS, 407, 846
Dressler, A. 1980, ApJ, 236, 351
Ehlert, S., von der Linden, A., Allen, S. W., et al. 2014, MNRAS, 437, 1942
Elbaz, D., Daddi, E., Le Borgne, D., et al. 2007, A&A, 468, 33
Fabian, A. C. 2012, ARA&A, 50, 455
Foreman-Mackey, D., Conley, A., Meierjurgen Farr, W., et al. 2013, emcee: The MCMC Hammer, Astrophysics Source Code Library, ascl:1303.002
Gabor, J. M., Capelo, P. R., Volonteri, M., et al. 2016, A&A, 592, A62
Gentile, F., Talia, M., Enia, A., et al. 2025, A&A, 697, A46
Gilli, R., Mignoli, M., Peca, A., et al. 2019, A&A, 632, A26
Gobat, R., Daddi, E., Coogan, R. T., et al. 2019, A&A, 629, A104
Hardcastle, M. J., Williams, W. L., Best, P. N., et al. 2019, A&A, 622, A12
Harrington, K. C., Vishwas, A., Man, A. W. S., et al. 2025, A&A, 701, A298
Heckman, T. M., & Best, P. N. 2014, ARA&A, 52, 589
Heckman, T. M., Roy, N., Best, P. N., & Kondapally, R. 2024, ApJ, 977, 125
Helou, G., Soifer, B. T., & Rowan-Robinson, M. 1985, ApJL, 298, L7
Heywood, I. 2020, oxkat: Semi-automated imaging of MeerKAT observations, Astrophysics Source Code Library, ascl:2009.003
Heywood, I., Jarvis, M. J., Hale, C. L., et al. 2022, MNRAS, 509, 2150
Hill, R., Chapman, S., Scott, D., et al. 2020, MNRAS, 495, 3124
Hill, R., Chapman, S., Phadke, K. A., et al. 2022, MNRAS, 512, 4352
Hughes, C., Hill, R., Chapman, S. C., et al. 2025, ApJL, 983, L11
Jonas, J. & MeerKAT Team 2016, PoS, 277, 001
Kamenetzky, J., Glenn, J., Rangwala, N., et al. 2012, ApJ, 753, 70
Kauffmann, G., White, S. D. M., Heckman, T. M., et al. 2004, MNRAS, 353, 713
Kenyon, J. S., Smirnov, O. M., Grobler, T. L., & Perkins, S. J. 2018, MNRAS, 478, 2399
Le Brun, A. M. C., McCarthy, I. G., Schaye, J., & Ponman, T. J. 2014, MNRAS, 441, 1270
Lehmer, B. D., Alexander, D. M., Chapman, S. C., et al. 2009, MNRAS, 400, 299
Li, Y., Wang, D.-X., & Gan, Z.-M. 2008, A&A, 482, 1
Mantz, A. B., Abdulla, Z., Allen, S. W., et al. 2018, A&A, 620, A2
Martini, P., Kelson, D. D., Kim, E., Mulchaey, J. S., & Athey, A. A. 2006, ApJ, 644, 116
McMullin, J. P., Waters, B., Schiebel, D., Young, W., & Golap, K. 2007, ASPC, 376, 127
McNamara, B. R., & Nulsen, P. E. J. 2007, ARA&A, 45, 117
McNamara, B. R., & Nulsen, P. E. J. 2012, NJPh, 14, 055023
Miller, T. B., Chapman, S. C., Aravena, M., et al. 2018, Natur, 556, 469
Nusser, A., Silk, J., & Babul, A. 2006, MNRAS, 373, 739
Offringa, A. R., McKinley, B., Hurley-Walker, N., et al. 2014, MNRAS, 444, 606
Oteo, I., Ivison, R. J., Dunne, L., et al. 2018, ApJ, 856, 72
Padovani, P. 2017, FrASS, 4, 35
Panessa, F., Baldi, R. D., Laor, A., et al. 2019, NatAs, 3, 387
Pentericci, L., Kurk, J. D., Carilli, C. L., et al. 2002, A&A, 396, 109

Pike, S. R., Kay, S. T., Newton, R. D. A., Thomas, P. A., & Jenkins, A. 2014, MNRAS, 445, 1774
Ponman, T. J., Cannon, D. B., & Navarro, J. F. 1999, Natur, 397, 135
Punsly, B. 2001, Black Hole Gravitohydromagnetics (2nd ed.; Springer)
Postman, M., Franx, M., Cross, N. J. G., et al. 2005, ApJ, 623, 721
Radcliffe, J. F., Barthel, P. D., Garrett, M. A., et al. 2021, A&A, 649, L9
Rasmussen, J., Mulchaey, J. S., Bai, L., et al. 2012, ApJ, 757, 122
Rasmussen, J., & Ponman, T. J. 2009, MNRAS, 399, 239
Rennehan, D., Babul, A., Hayward, C. C., et al. 2020, MNRAS, 493, 4607
Rotermund, K. M., Chapman, S. C., Phadke, K. A., et al. 2021, MNRAS, 502, 1797
Shi, X. 2016, MNRAS, 461, 1804
Smolčić, V., Novak, M., Delvecchio, I., et al. 2017, A&A, 602, A6
Sokołowska, A., Babul, A., Mayer, L., Shen, S., & Madau, P. 2018, ApJ, 867, 73
Sulzenauer, N., Weiß, A., Hill, R., et al. 2026, ApJ, 998, 191
Tasse, C., Hugo, B., Mirmont, M., et al. 2023, DDFacet: Facet-based radio imaging package, Astrophysics Source Code Library, ascl:2305.008
Thomson, A. P., Ivison, R. J., Simpson, J. M., et al. 2014, MNRAS, 442, 577
Tozzi, P., & Norman, C. 2001, ApJ, 546, 63
Tozzi, P., Pentericci, L., Gilli, R., et al. 2022, A&A, 662, A54
Travascio, A., Cantalupo, S., Tozzi, P., et al. 2025, A&A, 694, A165
Umehata, H., Fumagalli, M., Smail, I., et al. 2019, Sci, 366, 97
van Breukelen, C., Simpson, C., Rawlings, S., et al. 2009, MNRAS, 395, 11
van der Werf, P. P., Isaak, K. G., Meijerink, R., et al. 2010, A&A, 518, L42
Venkateshwaran, A., Weiss, A., Sulzenauer, N., et al. 2024, ApJ, 977, 161
Vito, F., Brandt, W. N., Comastri, A., et al. 2024, A&A, 689, A130
Vito, F., Brandt, W. N., Lehmer, B. D., et al. 2020, A&A, 642, A149
Wang, S. X., Brandt, W. N., Luo, B., et al. 2013, ApJ, 778, 179
Willott, C. J., Rawlings, S., Blundell, K. M., & Lacy, M. 1999, MNRAS, 309, 1017
Wilson, C. D., Rangwala, N., Glenn, J., et al. 2014, ApJL, 789, L36
Wu, K. K. S., Fabian, A. C., & Nulsen, P. E. J. 2000, MNRAS, 318, 889
Yang, H. Y. K., & Reynolds, C. S. 2016, ApJ, 829, 90
Zhou, D., Chapman, S. C., Sulzenauer, N., et al. 2025, ApJL, 982, L17
Zhou, D., Chapman, S., Aravena, M., et al. 2026, Natur, 649, 1130